Boosting Photoelectrochemical Water Splitting Performance of Ta_3N_5 Nanorod Array Photoanodes by Forming a Dual Co-catalyst Shell

Runze Chen[1,2,4†], Chao Zhen[2,3†], Yongqiang Yang[2,3], Xudong Sun[1,4], John TS Irvine,[5] Lianzhou Wang[6], Gang Liu[2,3*], Hui-Ming Cheng[2,7]

[1] Key Laboratory for anisotropy and Texture of Materials (Ministry of Education), Northeastern University, Shenyang, Liaoning 110819, China

[2] Shenyang National Laboratory for Materials Science, Institute of Metal Research, Chinese Academy of Sciences, 72 Wenhua Road, Shenyang 110016, China

[3] School of Materials Science and Engineering, University of Science and Technology of China, 72 Wenhua Road, Shenyang 110016, China

[4] Institute of Ceramics and powder Metallurgy, School of Materials Science and Engineering, Northeastern University, Shenyang, Liaoning 110819, China

[5] School of Chemistry, University of St. Andrews, Fife, KY16 9ST, UK

[6] Nanomaterials Centre, School of Chemical Engineering and AIBN, The University of Queensland, St Lucia, Brisbane, QLD 4072, Australia

[7] Tsinghua-Berkeley Shenzhen Institute, Tsinghua University, 1001 Xueyuan Road, Shenzhen 518055, China

† These authors equally contributed to this work.

*Corresponding author e-mail: gangliu@imr.ac.cn

Abstract

Concerning both the activity and stability of the promising solar-driven Ta_3N_5-based photoanodes for photoelectrochemical water splitting, the strategy for simultaneously promoting charge separation, enhancing catalytic activity and also improving the resistance to self-oxidation is highly desirable and actively pursued. In this study, a novel dual co-catalyst shell consisting of a continuous CoPi layer at the bottom and many non-continuous $Co(OH)_2$ islands at the top of the CoPi layer is designed to meet the strict requirements for efficient Ta_3N_5 photoanodes. As a result of the synergistic effects of such a shell in collectively addressing the concerns, the constructed photoanode of CoPi/$Co(OH)_2$-Ta_3N_5 nanorod arrays show the remarkably enhanced photoelectrochemical water splitting performance compared with the photoanodes with single co-catalyst. The results demonstrated in this study are expected to shed some light on constructing efficient photoelectrodes of the light absorbers that have wide absorption range but low resistance to self-oxidation.

Introduction

Converting and storing abundant solar energy into chemical bonds (e.g. H_2) has been regarded as an effective route to address the emerging issues of energy shortage and environmental pollution. Solar driven water splitting in the photoelectrochemical (PEC) cells is considered as a classic scenario for this purpose, and has been intensively investigated in the past decades.[1-8] The core part of a PEC cell is its photoelectrode, which performs the tasks of capturing incident sunlight to produce photogenerated charge carriers and subsequent inducing water splitting on its surface. Consequently, the materials for the photoelectrodes need to meet both thermodynamic and kinetic requirements in order to efficiently achieve solar-driven water splitting spontaneously as follows: 1) a proper bandgap between 1.6 and 2.0 eV that is desirable for water splitting with the purpose of fully utilizing sunlight; 2) appropriate band edge positions that stride over the redox potentials of water splitting; 3) high carrier transport ability that can enable the photo-carriers effectively to arrive at the surface; 4) active surface that can promote water splitting. Among numerous photoelectrode materials, n-type Ta_3N_5 with a direct bandgap of around 2.1 eV is one of a few ideal materials that almost fulfill all aforementioned requirements.[9,10] The theoretical solar to hydrogen storage efficiency of Ta_3N_5 based photoanodes was determined to be over 16%.[11]

On the basis of various strategies, very encouraging progress in developing efficient Ta_3N_5-based photoanodes [12-21, 24-27] has been made in the past decade. Although a record photocurrent density of 12.1 $mAcm^{-2}$ that is very close to the theoretical value of 12.9 $mAcm^{-2}$ under AM1.5G simulated sunlight has been achieved in the PEC cell

with interface-engineered Ta_3N_5 photoanodes,[12] the open voltages obtained so far are still much lower than the theoretical value.[12-15] The poor stability caused by the non-corrosion surface chemical reactions is another limiting factor of Ta_3N_5 based photoanodes. The self-limiting surface oxidation of Ta_3N_5 in aqueous solution results in a thin amorphous layer containing abundant oxygen, which is proved to pin surface Fermi level and thus fully suppressing the photoactivity of Ta_3N_5.[16] Conformal coating of a thin layer of oxygen evolution reaction (OER) co-catalyst on Ta_3N_5 photoanode surface can play a dual role in improving both the open voltage and stability by lowering the OER barrier and introducing water-proof shell. Various OER co-catalysts including CoO_x, $Co(OH)_2$, CoOOH, "CoPi" and Fe-Co-Ni based compounds have been extensively explored to decorate Ta_3N_5 photoanodes for performance improvement.[13,14,17-28] The formed interfaces (Ta_3N_5/co-catalyst and co-catalyst/electrolyte) accompanying with co-catalyst decoration play an important role in promoting the photo-carrier transfer, suppressing surface self-oxidation and thus improving the PEC water splitting performance. The rational designing of the Ta_3N_5/co-catalyst interface has attracted increasing attention and many modifiers that do not act as co-catalyst have also been attempted to further enrich the interface properties. Hole-storage layers (HSLs), ferrihydrite layer and $Ni(OH)_x$/ferrihydrite composite layer, formed at the Ta_3N_5/co-catalyst interface were demonstrated to be very effective in extracting photo-holes from Ta_3N_5 and delivering them to the OER co-catalysts.[12,14] Furthermore, a thin amorphous TiO_x layer introduced at the Ta_3N_5/HSL interface can act as an electron blocking layer to suppress the photocarrier recombination. By

conducting these interface designs, a record efficiency of 2.5 % with high photocurrent density of 12.1 $mAcm^{-2}$ was achieved by Li's group.[12] Alternatively, sequential deposition of co-catalysts with high hole-extraction ability and high OER activity is another effective strategy to facilitate interfacial transfer of photo-holes.[29] $Co(OH)_2$ has been recognized as an effective hole-extraction co-catalyst for Ta_3N_5 based photoanodes. Recently, the formation of interfacial Ta-O-Co bonds induced by the produced O* radicals under light irradiation was found to facilitate the photo-hole extraction for a high photocurrent density and good stability when high active OER co-catalyst "CoPi" was consecutively coated on the $Ta_3N_5/Co(OH)_2$ system.[30]

In this study, different from previous studies that used $Co(OH)_2$ as a photo-hole transfer bridge across the Ta_3N_5/CoPi interface,[27,30] we decorated $Co(OH)_2$ on the outermost surface of "CoPi" with the anticipation of enhancing the OER activity of "CoPi" to enable a better performance. Taking into account the potential advantages of one-dimensional array structures in capturing light, promoting charge separation and also modulating interface structures, the film of Ta_3N_5 nanorod arrays supported on Ta foil substrate was used as a platform to construct $Co(OH)_2$/CoPi-Ta_3N_5 photoanodes. Owing to the strong interaction between $Co(OH)_2$ and CoPi and enhanced OER activity at $Co(OH)_2$/CoPi/electrolyte three-phase boundaries, the resultant $Co(OH)_2$/CoPi-Ta_3N_5 photoanode shows the remarkably enhanced photocurrent density, open voltage and stability when compared with CoPi-Ta_3N_5 and $Co(OH)_2$-Ta_3N_5 photoanodes. The photocurrent density of the optimal $Co(OH)_2$/CoPi-Ta_3N_5 photoanode under AM 1.5G sunlight irradiation reaches 3.8 mA cm^{-2} at 1.23 V versus reversible hydrogen electrode

(RHE) and over 90% the initial value after a 20 min duration test.

Experimental section

Synthesis of Ta_3N_5 nanorod array films. Ta_3N_5 nanorod arrays supported on Ta foil substrate were synthesized by a template-free vapor-based hydrothermal process and subsequent high-temperature nitridation method according to our previous report.[15] In detail, Ta foil (0.25 mm thick, Alfa Aesar) was ultrasonically cleaned in ethanol, acetone, isopropanol and deionized water each for 15 minutes in series. The cleaned Ta foil was suspended above 0.2 M HF aqueous solution in a Teflon-lined autoclave, and heated at 180 ℃ for 12 h to grow Ta_2O_5 nanorod arrays on the Ta foil. After the vapor-phase hydrothermal reaction, the sample was heated in a gaseous NH_3 atmosphere with a flow of 20 mL/min at 1000 ºC for 6 h to form Ta_3N_5 nanorod arrays.

The deposition of $Co(OH)_2$ on Ta_3N_5 nanorods. The successive ionic layer adsorption and reaction method was used to deposit $Co(OH)_2$ nanoparticles onto the Ta_3N_5 nanorods. As-prepared Ta_3N_5 nanorod array photoanodes were immersed in an aqueous solution of 50 mM $Co(CH_3COO)_2$, deionized water, an aqueous solution of 100 mM NaOH and deionized water in turn each for 60 seconds to accomplish one cycle deposition of $Co(OH)_2$ nanoparticles. To get an optimal efficiency, five deposition cycles were repeated to load a desired amount of $Co(OH)_2$ nanoparticles on the nanorods.

The deposition of CoPi on Ta_3N_5 nanorods. Before the CoPi deposition, as-prepared nanorod array films were immersed in a mixed solution of $HF:HNO_3:H_2O$=1:2:7 in volume for tens of seconds and then rinsed with deionized water. The treated films were

deposited with CoPi cocatalysts by photo-assisted electrodeposition process,[13] which was conducted in a traditional three electrode photoelectrochemical cell (Ta_3N_5 photoelectrode as the working electrode, Ag/AgCl electrode as the reference electrode and a Pt foil as the counter electrode) with the electrolyte of 0.1 M potassium phosphate aqueous solution containing 0.5 mM $Co(NO_3)_2$ (pH = 7). During the 8 min photo-electrodeposition duration, a constant current density of 10 μA cm^{-2} was kept and the light irradiation was provided by an AM 1.5G sunlight simulator. After the deposition, the photoelectrode was rinsed with deionized water. In addition, the further deposition of $Co(OH)_2$ on CoPi-Ta_3N_5 was conducted by the procedures used for the deposition of $Co(OH)_2$ on bare Ta_3N_5 described above.

PEC water splitting measurement. The photoelectrochemical water splitting test was carried out in a three electrode system, in which the Ta_3N_5 nanorod array photoanode was used as the working electrode, Ag/AgCl electrode as the reference electrode and a Pt foil as the counter electrode. And the electrolyte is 1 M NaOH aqueous solution and the light source is AM 1.5G simulated sunlight (Newport). According to the Nernst equation ($E_{RHE}=E_{Ag/AgCl}+0.059\ pH + 0.196$), the recorded bias vs. Ag/AgCl reference electrode can be converted to potentials referring to RHE. The wavelength dependent incident photon-to-current conversion efficiency (IPCE) was calculated according to the following equation: IPCE(%) = [1240×photocurrent density (mA cm^{-2})] / [wavelength (nm) × photon flux (mW cm^{-2})] × 100%

Measurement of electrochemical impedance spectra. The electrochemical impedance spectra of samples were measured with an electrochemical work station

(Biologic VSP 300) at the potential of 1.23 V (vs. RHE) with a 10 mV amplitude perturbation and frequencies from 100 mHz to 1 MHz.

Measurement of gaseous products produced in the PEC water splitting. An airtight three-electrode PEC cell consisting of $Co(OH)_2$/CoPi-Ta_3N_5 photoanodes as the working electrode, Ag/AgCl electrode as the reference electrode and a Pt foil as the counter electrode was used for testing gas production. Prior to filling Ar gas in the cell to 5 kPa, the PEC cell was evacuated to less than 10 Pa. The PEC water splitting was conducted at 1.23 V vs. RHE in a stirred aqueous solution of 1 M NaOH under AM 1.5G simulated sunlight. The amount of hydrogen produced in the PEC cell was determined with a gas chromatograph (Agilent 6890N).

Results and Discussion

The successful synthesis of pure Ta_3N_5 phase was confirmed by X-ray diffraction (XRD) patterns of the as-prepared sample (Figure S1). No additional peaks appear in the XRD patterns after the deposition of CoPi and $Co(OH)_2$ as a result of the amorphous (or very low crystallinity) nature and low loading amount of these two components. Comparison of scanning electron microscopy (SEM) images of three modified Ta_3N_5 samples with pristine Ta_3N_5 (Figure 1a-c and Figure S2a) suggests no obvious change in the shape of the nanorods before and after the deposition of co-catalysts CoPi and/or $Co(OH)_2$, which indicates the conformal deposition of co-catalyst(s) on the Ta_3N_5 nanorods.

The microstructures of the nanorods in different samples were further characterized by recording transmission electron microscopy (TEM) images of single nanorod scraped from the Ta_3N_5 films. The nanorod from the pristine film has smooth surface

and a diameter of around 20 nm (Figure 1d). The corresponding high resolution TEM (HRTEM) image (Figure 1h) confirms the single crystalline nature of the nanorod and the lattice fringes with the spacing of 0.249 nm and 0.297 nm are corresponding to the (3-1-1) and (211) facets of Ta_3N_5, respectively. When CoPi was photo-deposited, an amorphous shell with a relatively uniform thickness of several nanometers was formed on the surface of the nanorod scraped from the CoPi modified Ta_3N_5 film (Figure 1e). The Ta_3N_5 nanorod and CoPi amorphous shell has a sharp interface and the single crystalline nature of the nanorod is well retained on the basis of the HRTEM image (Figure 1h). The uniformly and intimately coated CoPi shell has the dual functions of both extracting photo-holes and segregating Ta_3N_5 from water so that the performance and stability can be improved simultaneously. After subsequent deposition of $Co(OH)_2$ on the CoPi-Ta_3N_5 nanorods, additional particles with the size of several nanometers are randomly located on the outmost surface of the CoPi shell (Figure 1f). These small particles show blurry fringes with spacing of 0.276 nm and 0.178 nm (Figure 1i), which are associated with the (100) and (102) facets of $Co(OH)_2$. This suggests the formation of $Co(OH)_2$ nanoparticles on the outmost surface. Similar $Co(OH)_2$ nanoparticles are also observed on the Ta_3N_5 nanorods when $Co(OH)_2$ was directly deposited on the bare Ta_3N_5 nanorods (Figure S2b and c). In accordance with previous reports,[30] the $Co(OH)_2$ nanoparticles prepared by the successive ionic layer adsorption and reaction method are apt to form islands on the substrate. Such discontinuous shell consisting of the $Co(OH)_2$ islands is not effective in segregating Ta_3N_5 in the $Co(OH)_2$-Ta_3N_5 system from water. However, these $Co(OH)_2$ islands located on the uniform CoPi shell in

$Co(OH)_2$/CoPi-Ta_3N_5 can create numerous CoPi and $Co(OH)_2$ boundaries exposed. The strong interaction between the CoPi substrate and $Co(OH)_2$ nanoparticles might result in an enhanced OER catalytic activity at the boundaries.

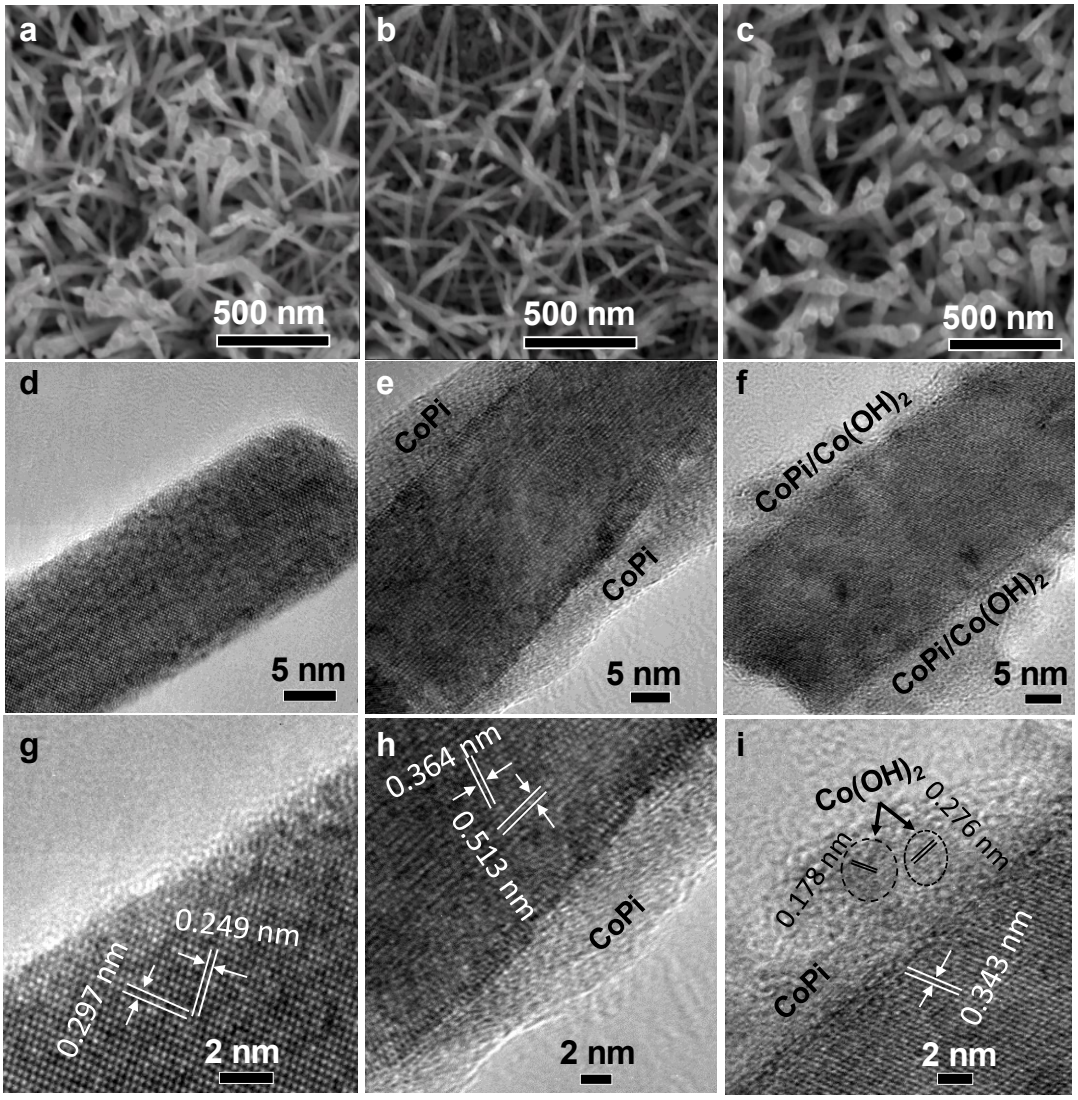

Figure 1. SEM images of the films of (a) bare Ta_3N_5, (b) CoPi-Ta_3N_5 and (c) CoPi/$Co(OH)_2$-Ta_3N_5 nanorod arrays. TEM and HRTEM images recorded from single nanorod scraped from (d, g) bare Ta_3N_5, (e, h) CoPi-Ta_3N_5 and (f, i) CoPi/$Co(OH)_2$-Ta_3N_5 films, respectively.

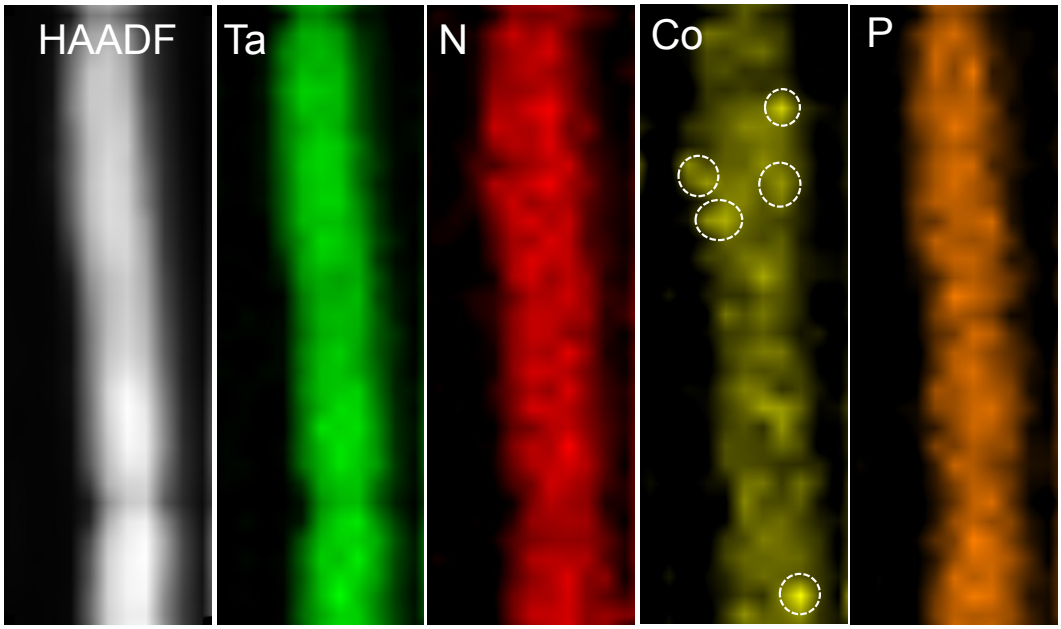

Figure 2. HAADF image of single nanorod scraped from CoPi/$Co(OH)_2$-Ta_3N_5 film and corresponding Ta element, N element, Co element and P element EDS mapping images recorded from the single nanorod.

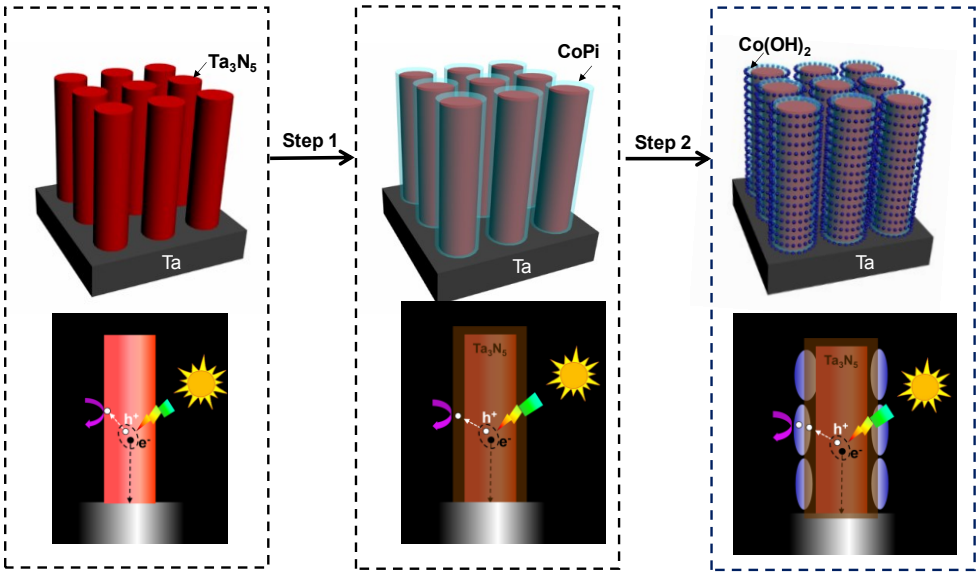

Figure 3. Schematic images of bare Ta_3N_5 nanorod arrays, CoPi decorated Ta_3N_5 nanorod arrays (CoPi-Ta_3N_5) and $Co(OH)_2$ decorated CoPi-Ta_3N_5 system (CoPi/$Co(OH)_2$-Ta_3N_5).

To further confirm the formation of isolated $Co(OH)_2$ islands on the well distributed CoPi shell, the elemental distribution images have been recorded on single nanorod scraped from the CoPi/$Co(OH)_2$-Ta_3N_5 film by TEM in the model of high angle annular dark-field (HAADF) with the help of energy dispersive spectrometer (EDS). The bright one-dimensional zone displayed in the HADDF image in Figure 2 (the left panel) corresponds to the CoPi/$Co(OH)_2$-coated Ta_3N_5 nanorod. Ta and N are two basic compositions of Ta_3N_5 so that their element mapping patterns duplicate the bright zone's shape of the nanorod. The signal of Co in the pattern is contributed by both CoPi and $Co(OH)_2$ and it exhibits a similar distribution pattern to that of Ta and N elements. This confirms the conformal deposition of CoPi and $Co(OH)_2$ on the Ta_3N_5 nanorods. To separate the distribution of the $Co(OH)_2$ nanoparticles from CoPi, P element, an exclusive composition P of CoPi is mapped to monitor the distribution of CoPi. The well-distributed P element indicates a uniform shell of CoPi on the Ta_3N_5 nanorod. The distribution of $Co(OH)_2$ can be recognized by comparing the difference between the mapping patterns of Co and P elements. The regions where Co element is present but P element absent correspond to the locations of $Co(OH)_2$, as selectively marked by the dashed circles in the Co mapping pattern. The distribution of $Co(OH)_2$ derived from the mapping patterns is consistent with the result from the HRTEM images. On the basis of all these structural characterizations above, the structure of the CoPi/$Co(OH)_2$-Ta_3N_5 photoanode studied here can be illustrated in Figure 3.

The PEC water splitting activities of the Ta_3N_5 photoanodes with different co-catalysts were tested in a three electrode system and details were described in the

experimental section. The bare Ta_3N_5 photoanode only delivered a photocurrent density of 0.25 mA cm^{-2} at 1.23 V (vs. RHE), and this value rapidly decayed to almost zero within only 400s (Figure 4). The photocurrent density at 1.23 V (vs. RHE) was improved to 1.7 mA cm^{-2} for the CoPi-Ta_3N_5 photoanode and an even higher value of 3.4 mA cm^{-2} was obtained with the $Co(OH)_2$-Ta_3N_5 photoanode. The greatly enhanced photocurrent density indicates that the photo-holes are effectively extracted from Ta_3N_5 light absorber to surface co-catalysts. The higher value achieved with $Co(OH)_2$ co-catalyst means that $Co(OH)_2$ has a higher photo-hole extraction ability compared with CoPi, which is in accordance with the previous report.[30] Despite of its higher activity, the $Co(OH)_2$-Ta_3N_5 photoanode exhibits a much faster photocurrent decay than the CoPi-Ta_3N_5 photoanode largely because of the poor ability of the non-continuous coating of $Co(OH)_2$ nanoparticles on the Ta_3N_5 nanorods in preventing the direct contact of water with Ta_3N_5. On the other hand, since the OER activity of CoPi is higher than that of $Co(OH)_2$, the photocurrent onset potential of the CoPi-Ta_3N_5 photoanode was more negative than that of the $Co(OH)_2$-Ta_3N_5 photoanode (797 mV vs 829 mV). What's more interesting is that the onset potential was further negatively shifted by 27 mV in the CoPi/$Co(OH)_2$-Ta_3N_5 photoanode (Figure S3). This clearly indicates that the synergistic effect of CoPi and $Co(OH)_2$ in enhancing OER activity. Comparison of the OER activities of the CoPi-Ta_3N_5 and CoPi/$Co(OH)_2$-Ta_3N_5 electrodes evaluated in dark in the same electrolyte **(Figure S4)** shows a more negative OER current onset potential of the latter, which doubly confirms the synergistic effect of two co-catalysts. As a consequence of both the enhanced OER activity and water proof capacity of the

continuous shell consisting of CoPi and $Co(OH)_2$ dual co-catalysts, the CoPi/$Co(OH)_2$-Ta_3N_5 photoanode has a highest photocurrent density of 3.8 mA cm^{-2} among all four photoanodes studied here and displays the high stability with less 10% photocurrent decay in a 20 min test duration. It's worth noting that there is an obvious oxidation peak in the J-V curve recorded on the $Co(OH)_2$-Ta_3N_5 photoanode, and the appearance of this oxidation peak results from the oxidation of $Co(OH)_2$ into CoOOH induced by photo-holes. It has been recognized that the $Co(OH)_2$/CoOOH redox potential (~0.65V vs. RHE) is much negative compared to the OER potential (1.23 V vs. RHE).[33] However, the redox couple potential of Co^{2+}/Co^{3+} in CoPi is ~1.1 V vs. RHE,[34] approaching to the OER potential, which is hardly oxidized and its corresponding oxidation-current peak is easily submerged in the photocurrent. Consequently, the oxidation-current peaks are absent in the J-V curves recorded on the CoPi-Ta_3N_5 and CoPi/$Co(OH)_2$-Ta_3N_5 photoanodes.

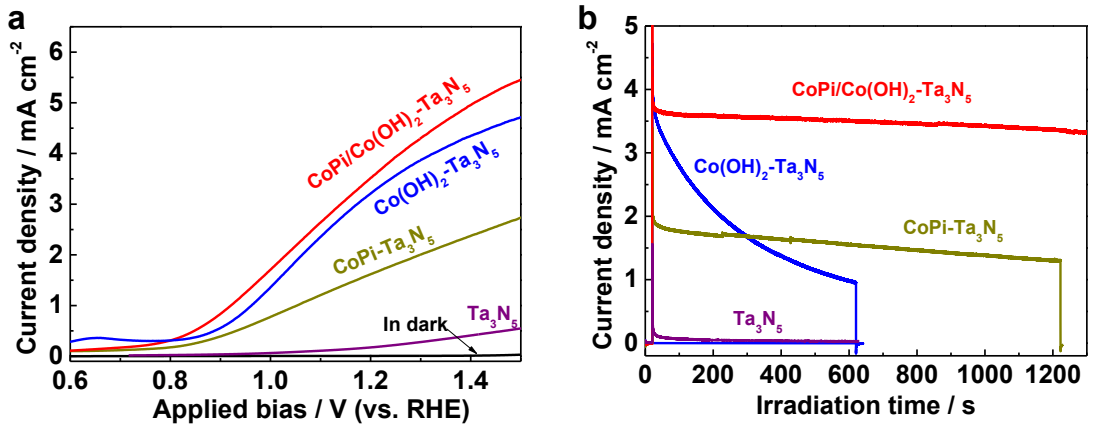

Figure 4. (a) J-V curves of bare Ta_3N_5, CoPi-Ta_3N_5, $Co(OH)_2$-Ta_3N_5 and CoPi/$Co(OH)_2$-Ta_3N_5 photoanodes tested under 1 sun simulator irradiation. (b) Time dependent photocurrent density at a fixed potential of 1.23 V vs. RHE.

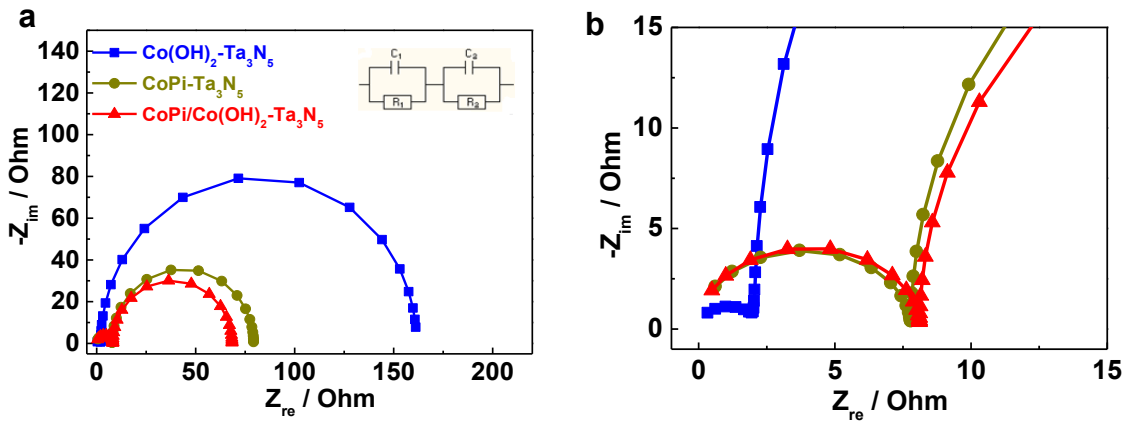

Figure 5. (a) Nyquist plots of the CoPi-Ta_3N_5, $Co(OH)_2$-Ta_3N_5 and CoPi/$Co(OH)_2$-Ta_3N_5 photoanodes tested under 1 sun simulator irradiation at a fixed potential of 1.23 V (vs. RHE). (b) Zoomed in Nyquist plots at high frequency range.

Electrochemical impedance spectra can provide important results to understand the carrier dynamics across the interfaces. Nyquist plots are commonly adopted to analyze the carrier interfacial transfer resistances in PEC cells,[31,32] and the number and diameter of the semi-arcs appearing in Nyquist plots indicate the number of existed interfaces and the carrier transfer resistances across different interfaces. In general, the smaller the diameter of a semi-arc is, the faster carrier transfer across the corresponding interface is. The Nyquist plots of three Ta_3N_5 photoanodes modified with co-catalysts were recorded under light illumination at a fix potential of 1.23 V (vs. RHE) (Figure 5). As the co-catalyst shell has been introduced in the photoanodes, two semi-arcs are commonly recorded in the Nyquist plots. They correspond to the carrier transfer across the Ta_3N_5/co-catalyst solid interface and co-catalyst/electrolyte (solid/liquid) interface. The small semi-arc at high frequency range reflects the information of carrier transfer across the Ta_3N_5/co-catalyst solid interface. To compare the carrier transfer resistance across the solid interface among different photoanodes, the high frequency range of the

Nyquist plots was zoomed in as shown in Figure 5b. The $Co(OH)_2$-Ta_3N_5 photoanode exhibits the smallest semi-arc at the high frequency range compared with the other two photoanodes. After fitting the Nyquist plots with a proper tandem equivalent circuit, the carrier transfer resistance across the $Co(OH)_2$-Ta_3N_5 interface is determined to be ~2.27 Ω, which is much lower than that (7.80 Ω) across the CoPi-Ta_3N_5 interface and that (8.11Ω) across the CoPi/$Co(OH)_2$-Ta_3N_5 interface. In contrast, the second semi-arc at low frequency range, which accounts for the carrier transfer resistance across the co-catalysts/electrolyte interface, is the biggest for the $Co(OH)_2$-Ta_3N_5 photoanode (127.1Ω) and followed by the CoPi-Ta_3N_5 (71.44Ω) and CoPi/$Co(OH)_2$-Ta_3N_5 (60.25Ω) photoanodes. This phenomenon means that the OER catalytic activity is the highest for CoPi/$Co(OH)_2$ and followed by CoPi and $Co(OH)_2$. The results derived from the electrochemical impedance spectra are in good agreement with the results from the J-V curves. The Nyquist plot fitted parameters by a tandem equivalent circuit (see the inset in Figure 5a) were summarized in Table S1.

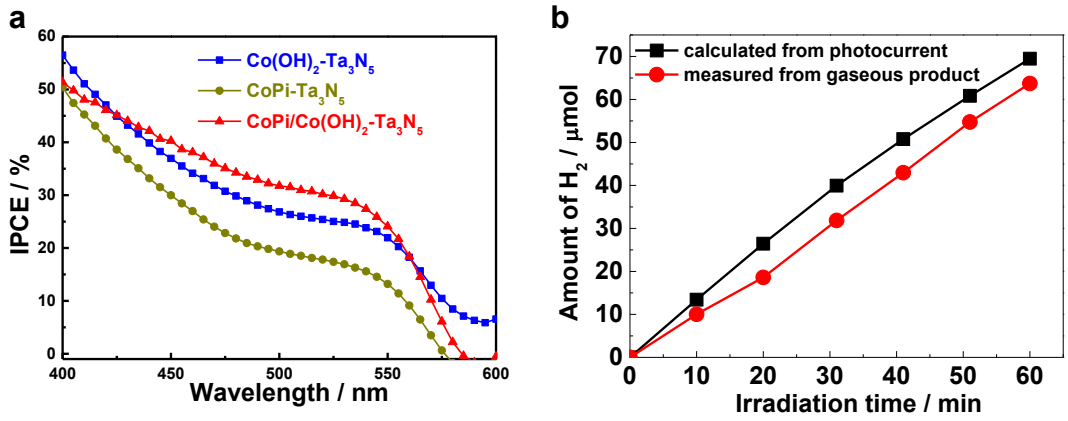

Figure 6. (a) IPCE spectra of the CoPi-Ta_3N_5, $Co(OH)_2$-Ta_3N_5 and CoPi/$Co(OH)_2$-Ta_3N_5 photoanodes. (b) Comparison of the amounts of H_2 calculated from the quantity of electric charge flow through the external circuit (black square) and H_2 generated in

the PEC cell (red circle).

The IPCE measurements were implemented to compare the wavelength dependent quantum efficiencies of the photoanodes. The curves of the quantum efficiency as a function of the wavelength of incident light for each photoanode in Figure 6a are similar to UV-visible absorption spectrum of the Ta_3N_5 matrix (Figure S5), suggesting that the photons absorbed at different wavelength regions can be utilized to excite valence band electrons for subsequent water splitting reaction. As the bandgap of Ta_3N_5 is ~2.1 eV, the photons with wavelength of <590 nm can be effectively absorbed and converted. The $Co(OH)_2$-Ta_3N_5 photoanode displays the higher quantum efficiencies in the whole responsive wavelength range as compared to the CoPi-Ta_3N_5 photoanode. Once the $Co(OH)_2$ was loaded on the CoPi-Ta_3N_5 photoanode, the resultant CoPi/$Co(OH)_2$-Ta_3N_5 photoanode exhibits the higher quantum efficiencies in the wavelength range from 425 to 560 nm in comparison with the $Co(OH)_2$-Ta_3N_5 photoanode. The obtained IPCE results are also consistent with the J-V measurements, where the CoPi/$Co(OH)_2$-Ta_3N_5 photoanode delivers the highest photocurrent density and the CoPi-Ta_3N_5 photoanode showed the lowest value. The relatively low quantum efficiencies in the region close to UV (400-420 nm) for the CoPi/$Co(OH)_2$-Ta_3N_5 photoanode may be caused by the co-catalyst shell that reduces light absorption of the Ta_3N_5 absorber. In addition, the $Co(OH)_2$-Ta_3N_5 photoanode delivers higher quantum efficiencies than two other photoanodes near the absorption edge range (550-600 nm), This abnormal phenomenon derives from the contribution of capacitive photocurrent from oxidizing

$Co(OH)_2$. As discussed on the J-V curves, $Co(OH)_2$ is easier to be oxidized into CoOOH by photo-holes from the Ta_3N_5 absorber compared to the water oxidation due to its more negative redox potential (~0.65 V vs, RHE), therefore, $Co(OH)_2$ has been frequently used as an promising material for supercapacitors.[35] The lower energetic photo-carriers induced by the long wavelength photons have the ability of oxidizing $Co(OH)_2$ and produce capacitive photocurrent, but they have a much lower capacity of oxidizing CoPi. So, it is believed that the higher IPCE of $Co(OH)_2$-Ta_3N_5 near the absorption edge range could result from the contribution of capacitive photocurrent from the oxidation of $Co(OH)_2$. The IPCE values of the CoPi/$Co(OH)_2$-Ta_3N_5 photoanode are higher than 30% before 540 nm. It is necessary to evaluate the Faraday efficiency of the efficient photoanode. The photocurrent produced by the CoPi/$Co(OH)_2$-Ta_3N_5 photoanode under one sun irradiation was recorded at a fixed potential of 1.23V (vs. RHE). To distinguish the effective current for water splitting from the recorded photocurrent, the amount of H_2 produced in the PEC test is compared with the theoretical amount of H_2 calculated from the recorded current in Figure 6b. The Faraday efficiency of the CoPi/$Co(OH)_2$-Ta_3N_5 photoanode is calculated to be higher than 90 %, indicating that most of the recorded photocurrent is associated with water splitting reaction.

Conclusion

By designing the shell consisting of a continuous CoPi layer at the bottom and many non-continuous $Co(OH)_2$ islands at the top of CoPi layer for the Ta_3N_5 nanorods, an efficient photoanode of CoPi/$Co(OH)_2$-Ta_3N_5 supported on Ta foil as the conductive

substrate for PEC water splitting is constructed. Owing to the remarkable functions of such a shell in segregating water from Ta_3N_5 to prevent self-oxidation of the nanorods and enhancing OER activity of co-catalysts together with the charge carrier separation, the constructed photoanode shows the greatly enhanced PEC water splitting performance in terms of activity and stability compared with three reference samples. The enhanced OER activity is largely attributed to the strong interaction between CoPi and $Co(OH)_2$ to create the boundaries associated active sites. At the bias of 1.23 V, the photoanode gives a photocurrent density of ~3.8 $mAcm^{-2}$ at 1.23 V (vs. RHE), and over 90% of the initial value can be retained after a 20 min stability test duration. The strategy shown here might be applicable to enhance the PEC performance of other light absorbers with wide absorption range but low resistance to self-oxidation.

Acknowledgments

The authors thank National Natural Science Foundation of China (Nos. 51825204，51572266, 21633009, 51629201), the Key Research Program of Frontier Sciences CAS (QYZDB-SSW-JSC039) for the financial support. G. L. is grateful for the award of the Newton Advanced Fellowship.

Reference

1 M. Grätzel, Nature 414 (2001) 338-344;

2 M.G. Walter, E.L. Warren, J.R. McKone, S.W. Boettcher, Q.X. Mi, E.A. Santori and N.S. Lewis, Chem. Rev. 110 (2010) 6446-6473;

3 Z.S. Li, W.J. Luo, M.L. Zhang, J.Y. Feng and Z.G. Zou, Energy Environ. Sci. 6 (2013) 347-370;

4 C. Zhen, R.Z. Chen, L.Z. Wang, G. Liu and H.M. Cheng, J. Mater. Chem. A 4 (2016) 2783-2800;

5 R.G. Li, Chin. J. Catal. 38 (2017) 5–12;

6 Z.L, Wang, L.Z. Wang, Chin. J. Catal. 39 (2018) 369–378;

7 T. Hisatomi, J. Jubota, K. Domen, Chem. Soc. Rev. 43 (2014) 7520-7535;

8 H.M. Chen, C.K. Chen, R-S. Liu, L. Zhang, J.J. Zhang, D. Wilkinson, Chem. Soc. Rev. 41 (2012) 5654–5671;

9 W.J. Chun, A. Ishikawa, H. Fujisawa, T. Takata, J.N. Kondo, M. Hara, M. Kawai, Y. Matsumoto and K. Domen, J. Phys. Chem. B 107 (2003) 1798-1803;

10 Z.H. Cui and H. Jiang, J. Phys. Chem. C 121 (2017) 3241-3251;

11 A.B. Murphy, P.R.F. Barnes, L.K. Randeniya, I.C. Plumb, I.E. Grey, M.D. Horne and J.A. Glasscock, Int. J. Hydrogen Energy 31 (2006) 1999-2017;

12 G.J. Liu, S. Ye, P.L. Yan, F.Q. Xiong, P. Fu, Z.L. Wang, Z. Chen, J.Y. Shi, and C. Li, Energy Environ. Sci. 9 (2016) 1327-1334;

13 Y.B. Li, L. Zhang, A. Torres-Pardo, J.M. Gonzalez-Calbet, Y. Ma, P. Oleynikov, O. Terasaki, S. Asahina, M. Shima, D. Cha, L. Zhao, K. Takanabe, J. Kubota and K. Domen, Nat. Commun. 4 (2013) 2566;

14 G.J. Liu, J.Y. Shi, F.X. Zhang, Z. Chen, J.F. Han, C.M. Ding, S.S. Chen, Z.L. Wang, H.X. Han and C. Li, Angew. Chem. Int. Edit. 53 (2014) 7295-7299;

15 M.X. Li, W.J. Luo, D.P. Cao, X. Zhao, Z.S. Li, T. Yu and Z.G. Zou, Angew. Chem. Int. Edit. 52 (2013) 11016-11020;

16 Y.M. He, J.E. Thorne, C.H. Wu, P.Y. Ma, C. Du, Q. Dong, J.H. Guo and D.W. Wang, Chem. 1 (2016) 640-655;

17 M.J. Liao, J.Y. Feng, W.J. Luo, Z.Q. Wang, J.Y. Zhang, Z.S. Li, T. Yu and Z.G. Zou, Adv. Funct. Mater. 22 (2012) 3066-3074;

18 Y.Q. Cong, H.S. Park, S.J. Wang, H.X. Dang, F.R.F. Fan, C.B. Mullins and A.J. Bard, J. Phys. Chem. C. 116 (2012) 14541-14550;

19 C. Zhen, L.Z. Wang, G. Liu, G.Q. Lu and H.M. Cheng, Chem. Commun. 49 (2013) 3019-3021;

20 Y.B. Li, T. Takata, D. Cha, K. Takanabe, T. Minegishi, J. Kubota and K. Domen, Adv. Mater. 25 (2013) 125-131;

21 M. Zhong, T. Hisatomi, Y. Sasaki, S. Suzuki, K. Teshima, M. Nakabayashi, N. Shibata, H. Nishiyama, M. Katayama, T. Yamada, K. Domen, Adv. Mater. 56 (2017) 4739-4734;

22 C. Zhen, T.T. Wu, M.W. Kadi, I. Ismail, G. Liu, H. M. Cheng, Chin. J. Catal. 36 (2015) 2171–2177;

23 Q.Z. Wang, T.J. Niu, L. Wang, J.W. Huang, S.D. She, Chin. J. Catal. 39 (2018) 613–618;

24 L. Pei, Z. Xu, Z. Shi, H. Zhu, S.C. Yan and Z.G. Zou, J. Mater. Chem. A 5 (2017) 20439-20447;

25 J.G. Hou, Z. Wang, C. Yang, H.J. Cheng, S.Q. Jiao and H.M. Zhu, Energy Environ. Sci. 6 (2013) 3322-3330;

26 L. Wang, F. Dionigi, N.T. Nguyen, R. Kirchgeorg, M. Gliech, S. Grigorescu, P. Strasse and P. Schmuki, Chem. Mater. 27 (2015) 2360-2366;

27 L. Wang, X.M. Zhou, N.T. Nguyen, I. Hwang, P. Schmuki, Adv. Mater. 28 (2016) 2432-2438;

28 A.A. Haleem, S. Majumder, N. Perumandla, Z.N. Zahran, Y. Naruta, J. Phys. Chem. C. 121 (2017) 20093-20100;

29 T.W. Kim and K.S. Choi, Science 343 (2014) 990-994;

30 Y.M. He, P.Y. Ma, S.S. Zhu, M.D. Liu, Q. Dong, J. Espano, X.H. Yao and D.W. Wang, Joule 1 (2017) 1-12;

31 Q. Wang, J.E. Moser and M. Gratzel, J. Phys. Chem. B 109 (2005) 14945-14953;

32 T. Lopes, L. Andrade, H.A. Ribeiro and A. Mendes, Int. J. Hydrogen Energy 35 (2010) 11601-11608;

33 R. Subbraraman, D. Tripkovic, Kee-Chul Chang, D. Strmcnik, A.P. Paulikas, P. Hirunsit, M. Chan, J. Greeley, V. Stamenkovic, N.M. Markovic, Nat. Mater. 11 (2012) 550-557;

34 M.K. Kanan, D.G. Nocera, Science 321 (2008) 1072-1075;

35 S. Gao, Y.F. Sun, F.C. Lei, L. Liang, J.W. Liu, W.T. Bi, B.C. Pan, Y. Xie, Angew. Chem. Int. Ed. 53 (2014) 12789 –12793.